

Synergistic improvements in mechanical and thermal performance of TiB_2 solid-solution-based composites

Zhuang Li(李壮), Cun You(由存), Zhihui Li(李志慧), Xuepeng Li(李雪鹏), Guiqian Sun(孙贵乾), Xinglin Wang(王星淋), Qi Jia(贾琪), Qiang Tao(陶强), and Pinwen Zhu(朱品文)

Citation: Chin. Phys. B, 2025, 34 (**8**): 086105. DOI: 10.1088/1674-1056/add00c
http://cpb.iphy.ac.cn; http://iopscience.iop.org/cpb

What follows is a list of articles you may be interested in

Heterogeneous TiC-based composite ceramics with high toughness

Xiaoci Ma(马孝慈), Yufei Ge(葛雨非), Yutong Hou(侯语同), Keyu Shi(施柯羽), Jiaqi Zhang(张佳琪), Gaoping Yue(岳高平), Qiang Tao(陶强), and Pinwen Zhu(朱品文)

Chin. Phys. B, 2025, 34 (**8**): 086104. DOI: 10.1088/1674-1056/add5c8

Prediction of superionic state in LiH_2 at conditions enroute to nuclear fusion

Fude Li(李福德), Hao Wang(王豪), Jinlong Li(李津龙), and Huayun Geng(耿华运)

Chin. Phys. B, 2023, 32 (**10**): 106103. DOI: 10.1088/1674-1056/acea68

Dependence of nitrogen vacancy color centers on nitrogen concentration in synthetic diamond

Yong Li(李勇), Xiaozhou Chen(陈孝洲), Maowu Ran(冉茂武), Yanchao She(佘彦超), Zhengguo Xiao(肖政国), Meihua Hu(胡美华), Ying Wang(王应), and Jun An(安军)

Chin. Phys. B, 2022, 31 (**4**): 046107. DOI: 10.1088/1674-1056/ac3220

Synthesis, structure, and properties of $Ba_9Co_3Se_{15}$ with one-dimensional spin chains

Lei Duan(段磊), Xian-Cheng Wang(望贤成), Jun Zhang(张俊), Jian-Fa Zhao(赵建发), Li-Peng Cao(曹立朋), Wen-Min Li(李文敏), Run-Ze Yu(于润泽), Zheng Deng(邓正), Chang-Qing Jin(靳常青)

Chin. Phys. B, 2020, 29 (**3**): 036102. DOI: 10.1088/1674-1056/ab69ea

Polycrystalline cubic boron nitride prepared with cubic-hexagonal boron nitride under high pressure and high temperature

Ming Yang(杨鸣), Zi-Li Kou(寇自力), Teng Liu(刘腾), Jing-Rui Lu(卢景瑞), Fang-Ming Liu(刘方明), Yin-Juan Liu(刘银娟), Lei Qi(戚磊), Wei Ding(丁未), Hong-Xia Gong(龚红霞), Xiao-Lin Ni(倪小林), Duan-Wei He(贺端威)

Chin. Phys. B, 2018, 27 (**5**): 056105. DOI: 10.1088/1674-1056/27/5/056105

SPECIAL TOPIC — Structures and properties of materials under high pressure

Synergistic improvements in mechanical and thermal performance of TiB_2 solid-solution-based composites

Zhuang Li(李壮), Cun You(由存), Zhihui Li(李志慧), Xuepeng Li(李雪鹏), Guiqian Sun(孙贵乾), Xinglin Wang(王星淋), Qi Jia(贾琪), Qiang Tao(陶强)[†], and Pinwen Zhu(朱品文)[‡]

Synergetic Extreme Condition High-Pressure Science Center, State Key Laboratory of High Pressure and Superhard Materials, College of Physics, Jilin University, Changchun 130012, *China*

(Received 26 February 2025; revised manuscript received 8 April 2025; accepted manuscript online 24 April 2025)

Continuously improving the mechanical properties of ultra-high-temperature ceramics (UHTCs) is a key requirement for their future applications. However, the mechanical properties of conventional UHTCs, HfB_2 and ZrB_2, remain unsatisfactory among transition metal light-element (TMLE) compounds. TiB_2 has superior mechanical properties compared to both HfB_2 and ZrB_2, but suffers from inherent brittleness and limited oxidation resistance. In this work, low-content solid-solution strengthening was used to fabricate dense samples of $Ti_x(Hf/Zr)_{1-x}B_2$ (THZ) under high pressure and high temperature (HPHT). Compared to pure TiB_2, $Ti_{0.94}(Hf/Zr)_{0.06}B_2$ exhibits a significant 38.8% increase in oxidation resistance temperature (950 °C), while $Ti_{0.91}(Hf/Zr)_{0.09}B_2$ shows a notable 28% enhancement in fracture toughness (5.8 MPa·m$^{1/2}$). The synergistic effect of a dual-atom solid-solution results in local internal stress and anomalous lattice contraction. This lattice contraction helps resist oxygen invasion, thereby elevating the oxidation resistance threshold. Additionally, the internal stress induces crack deflection within individual grains, enhancing toughness through energy dissipation. This work provides a new strategy for fabricating robust UHTCs within TMLE systems, demonstrating significant potential for future high-temperature applications.

Keywords: high pressure and high temperature, solid-solution strengthening, fracture toughness, oxidation resistance

PACS: 61.50.–f, 61.72.U–, 62.20.–x, 65.40.–b

DOI: 10.1088/1674-1056/add00c **CSTR:** 32038.14.CPB.add00c

1. Introduction

In recent years, extensive research and development efforts have focused on ultra-high temperature materials, including superalloys,[1] refractory metals,[2] and ultra-high temperature ceramics (UHTCs),[3,4] to address the escalating demands posed by extreme operating environments. Currently, ceramics used in extreme environments must not only possess excellent thermal resistance but also exhibit superior hardness and toughness. Transition metal (TM) diborides are recognized as exceptional UHTC materials due to their remarkably high melting points, and they have been regarded as promising candidates for leading-edge structures and hot components in aerospace applications.[5,6] In particular, HfB_2 and ZrB_2, as traditional UHTCs, have melting points above 3000 °C and initial oxidation temperatures around 1000 °C.[4] Although TiB_2 has a high melting point, its initial oxidation temperature is lower than that of other UHTCs, being only 466 °C as reported in previous studies.[7] However, TiB_2 possesses a hardness and toughness of 25 GPa and 4.0 MPa·m$^{1/2}$, which are much higher than those of HfB_2 (21.0 GPa and 3.2 MPa·m$^{1/2}$) and ZrB_2 (19.8 GPa and 2.9 MPa·m$^{1/2}$), and meet the current requirements of UHTCs for high hardness.[7–11] Although TiB_2 exhibits higher toughness compared to HfB_2 and ZrB_2, it is still brittle due to the presence of strong covalent bonds.[12] In the manufacturing sector, TiB_2-based cutting tools and wear-resistant parts exhibit longer service lives. The combination of high strength and relatively low density in TiB_2-based ceramics makes them attractive for light-weight structural applications. Therefore, further improvement of TiB_2 in terms of toughness and oxidation resistance is desirable for the development ceramics with excellent comprehensive performance.

There are many reports on how to improve the toughness of TiB_2-based ceramics. For example, metal sintering aids such as Fe, Ni, and ceramic additives such as SiC whiskers are employed to enhance the toughness of TiB_2-based materials.[13–16] Metal additives can improve toughness due to their inherent ductility. However, as a softer phase, they reduce the overall hardness of the material. Additionally, the lattice mismatch between SiC and TiB_2 results in weak grain boundary bonding, which reduces material strength. Compared to the TiB_2-SiC composite, which exhibits a toughness of 3.01 MPa·m$^{1/2}$, the $(TiZr)B_2$ solid-solution demonstrates a significantly higher toughness value of 5.2 MPa·m$^{1/2}$. Regarding fracture

[†]Corresponding author. E-mail: qiangtao@jlu.edu.cn

[‡]Corresponding author. E-mail: zhupw@jlu.edu.cn

© 2025 Chinese Physical Society and IOP Publishing Ltd. All rights, including for text and data mining, AI training, and similar technologies, are reserved.

strength, TiB_2-SiC composites have a value of only 431 MPa, while the (TiZr)B_2 solid-solution exhibits an impressive fracture strength of 558 MPa, reflecting nearly a 30% improvement.[15,27] Notably, improved densification,[13,17] enhancement of hardness[17–21] and fracture toughness,[17,18] and improved oxidation resistance,[13,22] have been achieved through the formation of boride solid-solutions.[17,21,23] These solutions can effectively overcome the limitations in mechanical, thermal, and other properties.[19,20,24–26] It is reported that single-phase solid-solutions, formed by solid-state reactions, exhibit superior toughness compared to two-phase mixtures.[27,28] Our previous studies have systematically established the mechanical enhancement mechanisms of low-concentration solid-solutions.[7,29,30] They demonstrated significant property improvements through controlled solute doping. Zhao *et al.*[30] found that low-concentration solid-solution can induce lattice distortion and local internal stress, which in turn leads to an enhancement in mechanical properties. Meanwhile, Zuo *et al.*[29] further revealed that this enhancement is not influenced by the charge density of the solute atoms. Therefore, the formation of a solid solution is a feasible strategy to improve the mechanical properties and high-temperature performance of TiB_2.

Materials with the same crystal structures and similar lattice parameters are more likely to form solid-solutions. HfB_2 and ZrB_2 share the same crystal structure and similar lattice parameters to TiB_2. Moreover, the melting points and initial oxidation temperatures are higher than those of TiB_2.[22,31–33] Consequently, introducing Hf and Zr atoms into the TiB_2 lattice could improve the mechanical properties through solution strengthening and lead to outstanding oxidation resistance. Based on these considerations, Hf and Zr atoms were selected to develop the $Ti_x(Hf/Zr)_{1-x}B_2$ (THZ) solid-solution, aiming to enhance both mechanical and thermal properties. In this work, we successfully prepared the THZ solid-solution under HPHT conditions, and the impact of different ratios of Hf and Zr on THZ ceramics was systematically investigated. It was found that low-concentration solid-solutions can enhance not only hardness but also toughness and oxidation resistance.

2. Experiment methods

Commercially available titanium boride (TiB_2, $\geq$ 99%, 1–5 μm), zirconium boride (ZrB_2, $\geq$ 99.5%, 100 × 325 mesh), and hafnium boride (HfB_2, $\geq$ 99%, 350 mesh) were all purchased from Shanghai Aladdin Co., Ltd., China and were used as raw materials. The ceramic composites in this study were designated as THZ3, THZ6, THZ9, and THZ12, corresponding to total mole percentages of HfB_2 and ZrB_2 in the initial formulation. The mole ratio of HfB_2 to ZrB_2 in the mixture was kept constant throughout. The powders were initially weighed in predetermined molar ratios, followed by ball milling using a ZrO_2-based jar on a planetary ball mill (FOCUCY, F-P400E, China) for 12 hours at a speed of 200 rpm to ensure homogeneous dispersion. In the ball milling process, ZrO_2 balls were used as the grinding media, with a ball-to-powder weight ratio of 20:1. Notably, no dispersant was added during the grinding procedure. After ball milling, the powder samples were sieved to ensure consistent particle size distribution.

Prior to HPHT synthesis, the ball-milled powder was compacted into cylinders ($\Phi = 4$ mm and $h = 2.5$ mm) under a pressure of 1 MPa to reduce porosity. The cylinders were subsequently enclosed within h-BN capsules to prevent sample contamination during the synthesis process. The HPHT synthesis was carried out using a 6 × 14400 kN cubic anvil apparatus under conditions of 5 GPa and 2000 °C, with a holding time of 30 minutes. Tungsten carbide anvils (23.5 mm ×23.5 mm face area) generated the high-pressure environment. The heater consisted of a graphite tube, and the temperature was calibrated in advance by a W5%Re–W26%Re thermocouple. The pressure was calibrated at room temperature by monitoring the diagnostic changes in the electrical resistances of Bi (at 2.55 GPa and 2.69 GPa) and Ba (at 5.5 GPa), which correspond to their respective semiconductor–metal phase transitions under high pressures. A pyrophyllite composite block was used as the pressure transfer medium (32.5 mm×32.5 mm×32.5 mm). MgO was used as an insulation material.

Before characterizing the sample, it was polished to remove surface impurities and ensure uniformity. The relative density of the sample was measured by the Archimedes method using ethanol as a medium. X-ray diffraction (XRD, Cu $K\alpha$, Smart-lab Rigaku, Japan) was used to analyze the phases and lattice information of the ball-milled powder and bulk samples after HPHT. The microstructures and elemental distribution of the polished surface and fracture surfaces were analyzed by scanning electron microscopy (SEM) and energy-dispersive spectroscopy (EDS) mapping (FEI Magellan 400 L). The Vickers hardness (HV) indentations of polished samples were collected at loading forces ranging from 0.49 N to 4.9 N using a microindentation hardness tester (HV-1000ZDT), and was calculated by[34]

$$H_{\mathrm{V}} = 1854.4 \times \frac{F}{d^2},$$

where F (N) is the corresponding loading force and d (μm) is the mean of the two diagonals of the indentation. Young's modulus (E) was tested on a nano indenter (G200, Keysight). The fracture toughness (K_{IC}) was determined by the indentation fracture method, which relies on cracks formed during HV testing. K_{IC} was calculated by[35]

$$K_{\mathrm{IC}} = 0.016 \times \sqrt{\frac{E}{H_{\mathrm{V}}}} \times \frac{F}{L^{\frac{3}{2}}},$$

where H_V is corresponding hardness, F is the corresponding applied load (N), and L is the average crack length (mean of L_1 and L_2, in mm).

3. Result and discussion

3.1. Characterization

To detect whether impurities were introduced during the ball milling and to analyze the phase composition after HPHT treatment, XRD was used. These results directly ensured the validity of the subsequent experimental analyses, by confirming both chemical purity and structural uniformity. Figures 1(a)–1(d) illustrate the XRD patterns of samples subjected to ball milling and HPHT with varying TiB_2 ratios. The data clearly demonstrate the structural evolution and phase composition changes with TiB_2 content. The XRD patterns of THZ samples after ball milling are presented in Fig. 1(a). The results show that all samples exhibit characteristic peaks corresponding to those of the standard reference cards (TiB_2:PDF#08-0121, HfB_2:PDF#06-0638, and ZrB_2:PDF#06-0610). This confirms the absence of impurities introduced during the milling process and indicates that no new phases were formed. Figure 1(b) shows the details of the area marked in Fig. 1(a), in the powders of THZ3, THZ6, and THZ9, the most intense diffraction peak appears at 44.53°, corresponding to the (101) crystal plane of TiB_2. However, when the molar content of TiB_2 was reduced to 88%, the dominant diffraction peak of the powder shifts, with HfB_2 becoming the primary contributor. Additionally, no separation or significant broadening of diffraction peaks was observed during the milling process, suggesting the structural integrity of the crystalline phases remained intact throughout.

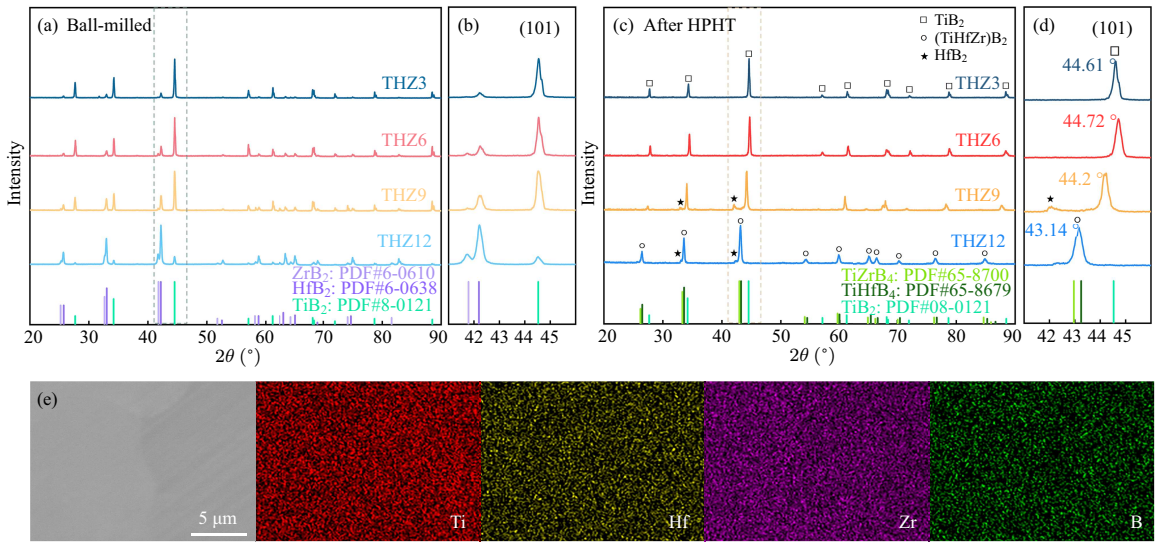


Fig. 1. (a) XRD results of the mixed raw ball-milled powders. (b) Enlarged view of the black dashed line box in (a). (c) XRD results of samples synthesized under HPHT with different TiB_2 ratios. (d) Enlarged view of the brown dashed line box in (c). (e) SEM image and EDS mapping of the polished surface of THZ ceramic.

XRD results of samples with different TiB_2 contents from 88% to 97% at 5 GPa and 2000 °C are shown in Fig. 1(c). After undergoing HPHT synthesis, the phase composition of the sample showed significant differences compared to the ball-milled powder. Specifically, THZ3 and THZ6 exhibit single-phase diffraction peaks, indicating a uniform crystal structure. However, when the HfB_2 and ZrB_2 content reaches 9%, the secondary phase emerges, evidenced by the appearance of a diffraction peak at 33.02°, corresponding to HfB_2. Reducing the TiB_2 content to 88% results in significant alterations in the primary diffraction peaks relative to higher compositions. A weak diffraction peak is also observed at 33.02°. The results obtained in this work suggest that the diffraction peaks of THZ3, THZ6, and THZ9 have similar values compared to TiB_2. However, these samples exhibit significant peak shifts, indicating subtle structural adjustments. In contrast, the diffraction pattern of THZ12 aligns with a new single-phase solid-solution, suggesting a more substantial transformation in the crystallographic structure. Figure 1(d) clearly shows that the key peaks for the THZ3, THZ6, and THZ9 are located at 44.61°, 44.72°, and 44.20°, respectively, corresponding to the (101) plane of TiB_2. The analysis confirms the establishment of a stable solid-solution. THZ12 showed a deviated significantly from that of TiB_2, with its key diffraction peak located at 43.14°. This position, lying between the key diffraction peaks of $(Ti_{0.5}Zr_{0.5})B_2$ (PDF#65-8700) and $(Ti_{0.5}Hf_{0.5})B_2$ (PDF#65-8679) solid-solutions, provides direct evidence for the formation of the $(Ti/Hf/Zr)B_2$ solid-solution within THZ12. The variations in composition result in differences in the lattice structure of the synthesized samples. The introduction of Hf and Zr atoms into the solid-solution modifies the lattice structure, leading to a shift in the XRD diffraction peaks (Fig. 1(d)). Typically, Hf and Zr atoms possess larger atomic radii compared to Ti atoms. Consequently,

when Ti atoms in the TiB_2 lattice are replaced with Hf or Zr, the lattice is expected to expand. However, contrary to expectations, the doping process results in a slight lattice contraction. Interestingly, this contraction halts once the Hf and Zr doping content reaches 9%. This phenomenon can be attributed to the synergistic effect of dual-atom solid-solution, which generates localized internal stress and leads to anomalous lattice contraction. Hf and Zr exhibit higher electronegativity than Ti, leading to stronger covalent bonding with boron. This strengthening of the B-TM bonds pulls the atoms closer together, thereby reducing the lattice parameters. Notably, the increased bond strength surpasses atomic size effects, resulting in an overall contraction of the lattice. This demonstrates that the strengthening of chemical bonds can dominate over atomic size effects, leading to a net reduction in lattice parameters. When the substitution level exceeds 9%, Hf and Zr atoms no longer fully occupy Ti lattice sites, as evidenced by the emergence of secondary HfB_2 peaks observed in THZ9 (Fig. 1(c)). These observations suggest that lattice expansion only occurs at higher doping levels.

3.2. Microstructure and mechanical properties

The elemental distribution on the polished surface of the THZ samples sintered under HPHT can be seen in Fig. 1(e). It can be observed that the four elements reveal a uniform distribution of all four elements without noticeable segregation. The combined results of XRD, SEM, and EDS analyses confirmed the formation of a complete solid-solution. SEM images depicting the fracture surfaces of the THZ3, THZ6, THZ9, and THZ12 compositions are presented in Figs. 2(a)–2(d), while crack propagation on the polished surfaces of THZ6 and THZ9 is shown in Figs. 2(e) and 2(f). After HPHT treatment, the grains in the samples appear tightly bonded, exhibiting excellent densification and an absence of porosity. The observed microstructures analysis of the fracture surfaces of the solid-solutions are consistent with the relative density values measured by the Archimedes method, as presented in Table 1. The grain sizes across all samples remain within the micron scale. Moreover, as the content of HfB_2 and ZrB_2 increases, a gradual refinement in grain size is observed. This is mainly due to the coupling effect of solid-solution reactions and composite phases during the reaction, which promote densification and inhibit grain growth.[24,25,27] Notably, Fig. 2(c) reveals the presence of elongated grains (marked in a blue box) between the boundaries, which are considered to play a crucial role in grain boundary pinning to enhance the sample's toughness. Figure 2(d) illustrates the microstructure of the THZ9 solid-solution, where significant grain refinement is evident. Although more pores are observed than in the other three samples, the overall structure remains dense and compact.

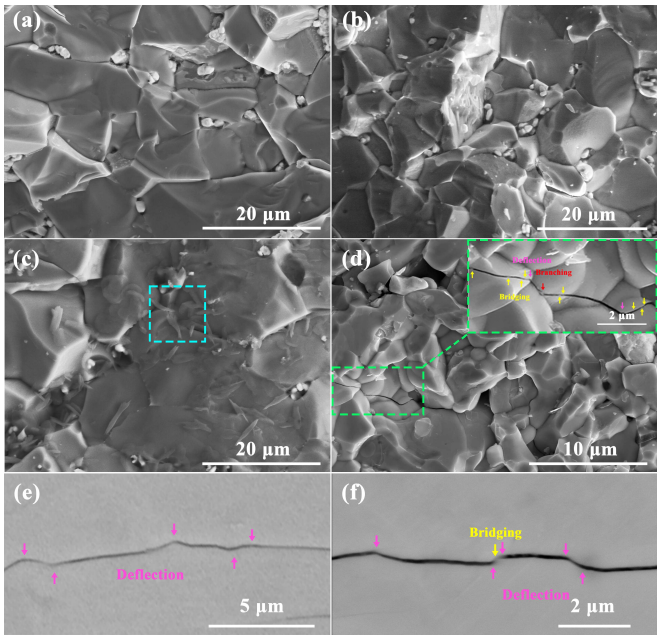


Fig. 2. (a)–(d) SEM images of the fracture interface of bulk samples with different TiB_2 contents: (a) THZ3, (b) THZ6, (c) THZ9, and (d) THZ12. (e) Crack propagation on the polished surface of THZ6. (f) Crack propagation on the polished surface of THZ9. The blue box in (c) indicates the presence of elongated grains in THZ9. The green box in (d) shows the crack propagation on the fracture surface of THZ12.

Table 1. Sintering conditions under HPHT, relative densities *RD*, Vickers hardness H_V, fracture toughness K_{IC}, oxidation temperature T_C, and Young's modulus *E*.

Samples	Pressure (GPa)	Temperature (°C)	*RD* (%)	H_V (GPa)	K_{IC} (MPa·m$^{1/2}$)	T_C (°C)	*E* (GPa)
THZ3	5	2000	98.9	26.1±0.45	4.8±0.45	923	554.2±23.4
THZ6	5	2000	99.4	26.8±0.40	5.5±0.53	950	562.5±27.3
THZ9	5	2000	99.1	25.9±0.43	5.8±0.60	920	544.7±25.2
THZ12	5	2000	98.2	24.2±0.57	5.1±0.77	915	539.7±32.1
TiB_2	5	2000	98.5	25.1±0.61	4.5±0.89	581	556.8±29.8
HfB_2[7,40,41]	–	–	98.0	21.0	3.2	724	–
ZrB_2[7,10,41]	–	–	98.0	19.8	2.9	632	–
TiB_2[7]	5	1600	–	25.0	–	466	–
TiB_2[42]	3	2477	98.0	24.5	3.9	–	–

To probe atomic-scale structural details, transmission electron microscope (TEM) was employed to systematically characterize the crystal structure, microstructural evolution, and compositional homogeneity of the THZ composites. Figures 3(a) and 3(c) show bright-field images of THZ6 and THZ9 particles with reduced thickness, which facilitates the analysis of their crystal structure. Figure 3(b) shows a high-resolution TEM (HRTEM) image, in which a periodic struc-

ture is observed, featuring two sets of fringes with interplanar spacings of approximately 1.47 Å and 1.48 Å respectively, corresponding to the (110) plane of THZ6. The (110) interplanar spacing of the THZ6 ceramics is close to, but not identical to, that of pure TiB_2 (1.51 Å), further confirming the formation of a solid-solution phase during the composite fabrication process. This observation suggests that THZ6 underwent a slight lattice contraction relative to pure TiB_2. The decrease in interplanar spacing implies the incorporation of Hf and Zr into the TiB_2 lattice. This contraction is likely caused by electronic interactions related to the specific doping concentrations of Hf and Zr. Figure 3(d) is the HRTEM of THZ9 and the (202) plane of THZ9 with the interplanar spacing of 1.06 Å is resolved. Similarly, the crystal plane spacing of THZ9 ceramics differs slightly from that of the (202) plane of pure TiB_2, indicating the presence of some lattice distortion in the solid solution. These distortions contribute to the enhancement of the mechanical properties.

Understanding the evolution of mechanical properties in composites with varying TiB_2 ratios is essential for elucidating the mechanisms underlying their hardening and toughening behaviors. Figure 4(a) depicts the evolution of hardness curves for all samples. The hardness initially increases with incremental additions of HfB_2 and ZrB_2 but decreases beyond a critical concentration. When the combined content of HfB_2 and ZrB_2 reaches 6%, the hardness value reaches its maximum at 26.8 GPa, after which a decline is observed. This phenomenon of high hardness is intimately linked to the high density exhibited by the sample and the compact microstructure revealed in Fig. 2. At a concentration of 9%, the hardness value is 25.9 GPa, and XRD results show that a secondary phase of HfB_2 was detected. Reported values indicate that the hardness value for HfB_2 is 21.5 GPa, while that of TiB_2 reaches 25 GPa, highlighting the superior mechanical properties of TiB_2.[2] The reduction in hardness may be attributed to two primary factors: one is that HfB_2 inherently exhibits lower hardness than a TiB_2-based phase;[7,9,36] the other is that the reduction in relative density further contributes to the decline in hardness. These combined effects diminish the overall mechanical performance of the material. The primary phase of THZ12 shifted from a TiB_2-based solid-solution to $(Ti/Hf/Zr)B_2$ solid-solution. Previous studies have demonstrated that ternary solid-solutions of $(Ti/Hf/Zr)B_2$ exhibit a hardness of approximately 23 GPa, which is significantly lower than that of pure TiB_2.[37] The relatively low density, at only 97.3%, combined with the presence of a softer phase, results in a reduction of the overall hardness, bringing the hardness below 25 GPa. However, the hardness is still comparable to that of pure TiB_2. In addition, the hardness of all THZ ceramics is significantly higher than that of the single-phase HfB_2 and ZrB_2.

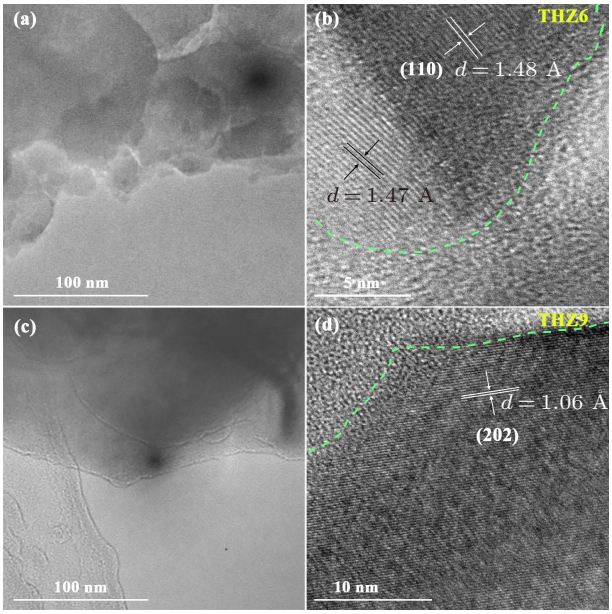


Fig. 3. (a) and (b) TEM images and HRTEM images of THZ6; (c) and (d) TEM images and HRTEM images of THZ9.

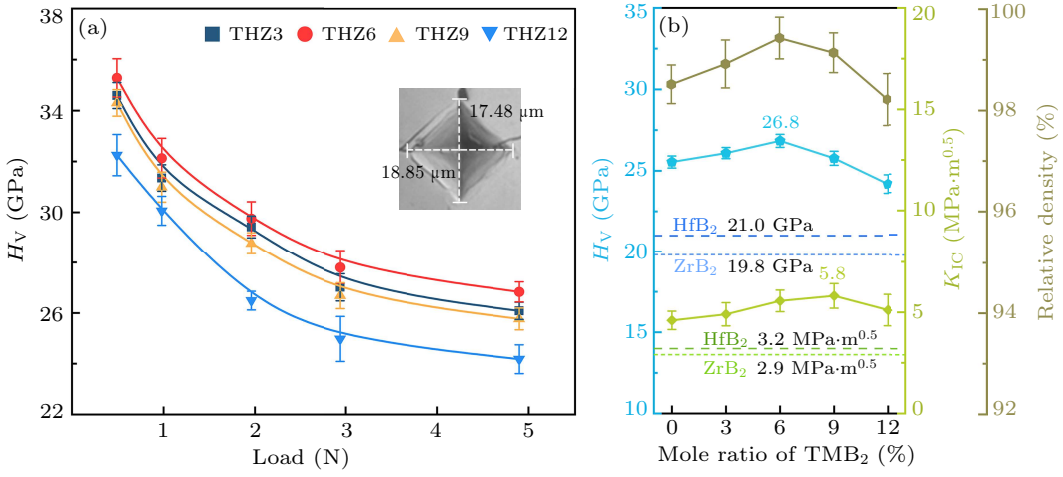


Fig. 4. (a) The Vickers hardness curves of all samples, and an indentation on the polished surface of THZ6 under a 500 g load. (b) The relationships between Vickers hardness, fracture toughness, relative density, and the combined molar ratio of HfB_2 and ZrB_2.

Figure 4(b) shows the changes in hardness, toughness, and density of samples with different component contents. The Young's modulus (E) was determined using nanoindentation, and the load-displacement curve obtained from the nanoindentation process is presented in Fig. 5. Among all the samples, THZ6 exhibits the highest hardness, with a Young's modulus of 562 GPa. THZ9 demonstrates the best toughness and has a Young's modulus of 544 GPa. The trend in Young's modulus aligns with that of hardness. While Young's modulus and hardness are distinct properties, they may be influenced by common factors such as material composition, microstructure, and bonding characteristics. This results in similar trends in their variation. The fracture toughness exhibited an initial increase followed by a subsequent decrease as the total content of HfB_2 and ZrB_2 progressively increased from 3% to 12%, indicating a non-linear relationship. When the total content of HfB_2 and ZrB_2 was 3%, there is no significant increase in toughness. This is attributed to the relatively limited content of HfB_2 and ZrB_2, which results in negligible lattice distortion. Consequently, the hardness and toughness show only slight improvement, as the slight structural changes are insufficient to substantially enhance its mechanical properties. The XRD patterns of THZ6 samples exhibit more evident peak shifts, indicative of greater lattice distortion. Such distortion facilitates enhanced energy absorption during the fracture process, which in turn contributes to a marked improvement in toughness. When the combined content of HfB_2 and ZrB_2 reaches 9%, the toughness of the material reaches a peak of 5.8 MPa·m$^{1/2}$, compared to pure TiB_2, its toughness is approximately 28% higher. Compared to HfB_2 and ZrB_2, the toughness increases by over 81% (as shown in Table 1). Therefore, the toughness of THZ ceramics surpasses that of any single-phase TMB_2 material. This enhancement in toughness is attributed to the formation of elongated grains, which help improve the mechanical ability to absorb energy and resist fracture. As noted in prior research, the incorporation of whisker-like or plate-shaped grains into ceramics can significantly enhance toughness through such crack-deflection and grain bridging mechanisms.[27,38,39] Consistent with these findings, the elongated, flaky grains observed in THZ9 also enhanced the toughness of ceramics. These grains promote crack deflection and generate a pinning effect at the grain boundaries, effectively restricting crack propagation and improving mechanical resilience. Lattice distortion and prestress can also deflect crack propagation within the grain, and dissipate fracture energy. The green box in Figs. 2(d)–2(f) illustrates the crack propagation characteristics in the THZ6, THZ9, and THZ12 samples, where two distinct fracture modes, inter-granular and trans-granular fracture, coexist. The crack propagation follows a complex zigzag path, featuring mechanisms such as crack deflection, crack bridging, and branching, as shown in the SEM results. These mechanisms effectively enhance the toughness of the samples by redistributing stress, dissipating fracture energy, and resisting crack propagation. As illustrated in Figs. 2(e) and 2(f), the crack propagates along a deflected path within individual grains due to localized internal stresses, with such stress-induced crack deflection contributing to the material's superior toughness through enhanced crack path tortuosity.

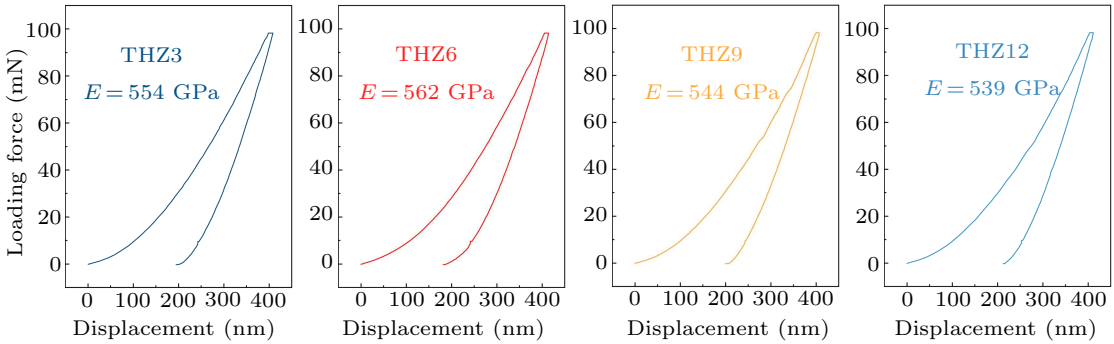


Fig. 5. Nanoindentation measurements of THZ ceramics.

3.3. Oxidation resistance of THZ ceramics

The oxidation performance is a critical factor in assessing the suitability of UHTCs for applications in extreme environments. The oxidation resistance of different ceramics sintered under HPHT conditions was assessed via thermal analysis in air at a heating rate of 10 °C/min up to 1300 °C. All specimens retained their macrostructure integrity after the oxidation tests. As previously reported, HfB_2 and ZrB_2 exhibit higher initial oxidation temperatures compared to TiB_2,[7] indicating that incorporating them into TiB_2-based materials via solid-solution is an effective strategy for enhance oxidation resistance. The variation in weight as a function of temperature is shown in Fig. 6(a). The oxidation process of TM diborides follows

$$TMB_2(s)+\frac{5}{2}O_2(g) \rightarrow TMO_2(s)+B_2O_3(l).$$

Initially, a slight weight loss is observed in the thermogravimetric (TG) curve, which is attributed to the volatilization of

surface impurities and moisture. The TG analysis identifies two parts in the weight gain rate as the temperature increases from room temperature to 1300 °C, corresponding to two successive oxidation stages. The first stage, occurring beyond 600 °C, is primarily attributed to the reaction of TM diborides with oxygen, resulting in the formation of TM oxides (TMO_2) and liquid B_2O_3. The latter forms a dense, protective film covers the sample surface, effectively mitigating the oxidation rate during this stage. The second stage occurs above 900 °C. Moreover, as the temperature exceeds 900 °C, the evaporation of B_2O_3 leads to a steep increase in the TG curve slope, indicating an accelerated oxidation process.[10,25,37] Both oxidation stages are observed across the four samples, with slight numerical differences. Figure 6(b) compares the histograms of the oxidation temperature for the four samples. The data reveal that both critical temperatures exhibit a trend of increasing initially and then decreasing as the HfB_2 and ZrB_2 total content rises. Among these, the THZ6 sample achieves the highest critical temperatures, with 650 °C for the initial oxidation and 950 °C for the second-stage oxidation, representing the best thermal performance among the four samples. The initial oxidation temperature of pure TiB_2 has been reported to be 466 °C in previous studies,[7] while our research shows it to be 581 °C. Furthermore, it is worth noting that the initial oxidation temperature of the THZ6 solid-solution ceramics is 12% higher than that of pure TiB_2. This represents an increase of 38.8% in oxidation resistance temperature (950 °C). This is primarily due to the presence of prestress, which induces lattice-contraction as previously discussed, thereby hindering the ingress of oxygen atoms and preventing lattice damage. The slight decrease in the initial oxidation temperature of THZ9 and THZ12 is due to the reduced density, as previously measured. Additionally, as demonstrated by XRD and HRTEM results, the lattice expansion of THZ9 and THZ12 leads to a reduced capacity to impede oxygen atoms, thereby resulting in diminished oxidation resistance. Therefore, the incorporation of the solid-solution composite phase can significantly improve the antioxidant properties of TiB_2-based ceramics.

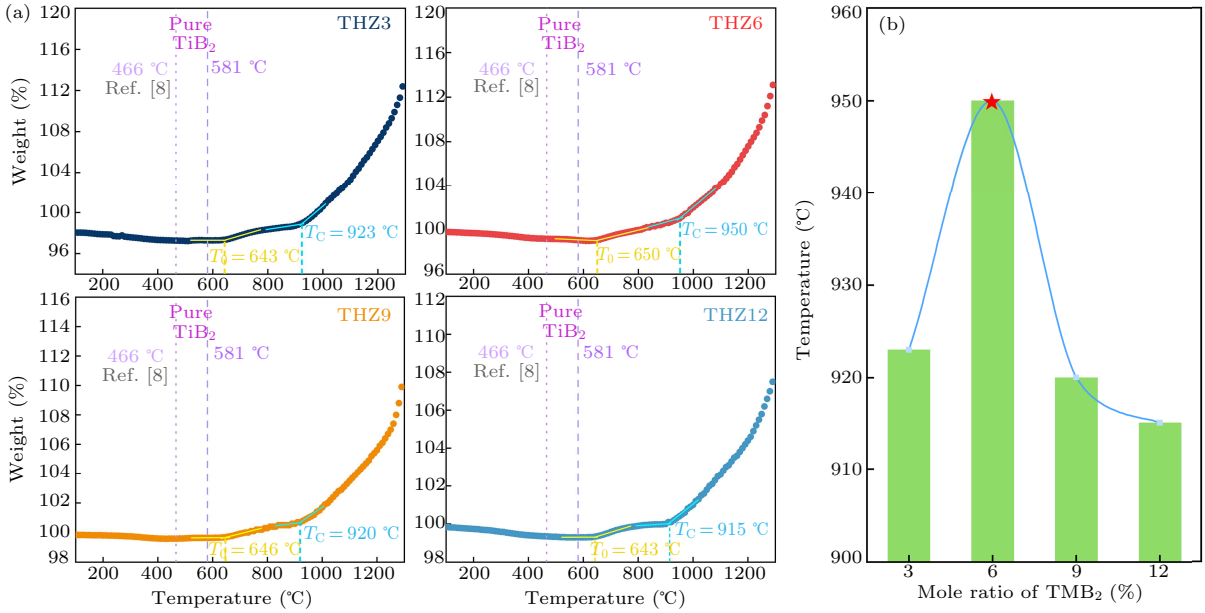


Fig. 6. (a) Thermogravimetric curves for all samples, T_0 represents initial oxidation temperature and T_C represents the critical oxidation temperature. The purple dashed line indicates the initial oxidation temperature of pure TiB_2 as reported in both the literature and this study. (b) Oxidation temperatures for all samples with different TiB_2 content.

To more intuitively observe the changes in the sample surface after oxidation, the macroscopic images of cross-sections of all samples oxidized in air up to 1300 °C are presented in Figs. 7(a)–7(d). SEM and EDS analyses revealed that a layer of oxide formed on the surface following heat treatment. Furthermore, variations in oxygen partial concentration across different depths of the sample during the oxidation process resulted in the formation of three distinct layers within the oxidized sample, each characterized by varying degrees of oxidation. The first layer consists of a loose TMO_2 formed after the volatilization of B_2O_3 above 900 °C. The SEM results show that the grains in the second layer are more densely packed and finer in structure. The formation of the second layer occurs when the first layer is no longer capable of resisting oxygen erosion. Compared to the first oxide layer, the second oxide layer plays a more significant role in grain refinement and densification. The increasing heating temperature led to the densification of TMO_2, which prevents further oxidation. This refined structure enhances resistance to oxygen diffusion, effectively acting as a barrier that limits oxygen from penetrating deeper into the material. As a result, the second oxide layer slows down the progression of oxygen erosion,

providing an additional protective mechanism to maintain the integrity. The third layer, identified as the ceramic matrix, exhibits a micromorphology consistent with that observed in samples not subjected to heat treatment. In THZ6, the dual-atom solid-solution facilitates the formation of a dense and continuous TMO_2 oxide layer (Fig. 7(b)), which effectively impedes oxygen diffusion. In contrast, the higher Hf and Zr content in THZ9 disrupts this uniformity, and the volatilization of B_2O_3 at 900 °C exposes the relatively loose TMO_2 (Fig. 7(c)), thereby reducing the protective efficacy of the oxide layer. The EDS results indicate that metal elements are present in all layers. Oxygen is primarily concentrated in the first layer, with a smaller presence in the second layer, and only trace amounts detected throughout the matrix (marked with circle). Compared to THZ6, THZ9 matrix exhibits a significantly higher oxygen content, as evidenced by our elemental analysis results, which further support the high oxidation resistance of THZ6. The notably rare distribution of B elements in the first layer, compared to the other two layers, can be attributed to the volatilization of B_2O_3 during heat treatment. These EDS results correspond to the results of the thermogravimetric analysis. The oxidation temperature of the samples in this study is markedly higher than that of previously reported pure-phase TiB_2. On the one hand, this can be attributed to the densification of the second TMO_2 layer by the increasing heating temperature, which prevents further oxidation. On the other hand, the synergistic interaction between the solid phase and the composite phase generates numerous microstructures within the samples, which may produce prestress to restrain further oxidation, demonstrating their potential for applications in extreme environments.

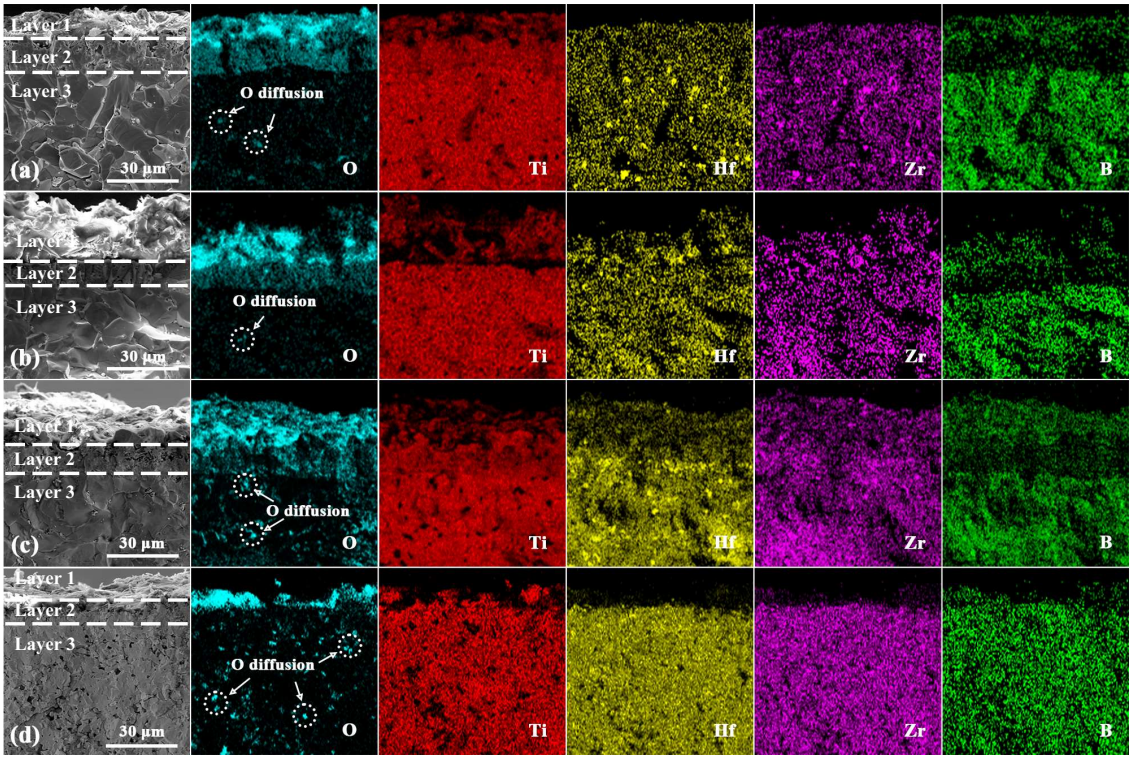


Fig. 7. (a)–(d) SEM and EDS images of the cross-sections of THZ ceramics oxidized at 1300 °C: (a) THZ3, (b) THZ6, (c) THZ9, and (d) THZ12. The circles represent the diffusion of oxygen within the matrix.

4. Conclusion

In summary, THZ solid-solution with optimized comprehensive properties was synthesized. The highest densification (99.4%), and hardness (26.8 GPa) were achieved in THZ6. The oxidation temperature of THZ6 is 950 °C, representing a 38.8% increase compared to pure TiB_2. THZ9 exhibits fracture toughness of 5.8 $MPa{\cdot}m^{1/2}$, which is 28% higher than TiB_2 and 81% higher than HfB_2 and ZrB_2. The lattice dislocations and the local internal stress caused by solid-solution not only enhanced the hardness but also significantly promoted crack deflection in individual grains and then improving the fracture toughness. Regarding oxidation resistance, the presence of prestress induces lattice contraction, thereby hindering the ingress of oxygen atoms. Furthermore, surface-layer grains were oxidized into fine TMO_2, which densified at a relatively low temperature, forming a continuous protective layer that effectively inhibits further oxygen diffusion. Overall, the synergistic effect of the dual-atom solid-solution provides an effective way to enhance the comprehensive performance.

Acknowledgements

The high-pressure experiments were conducted at the B1 station, Synergetic Extreme Condition User Facility (SECUF). The authors acknowledge funding support from the Program for the Development of Science and Technology of Jilin Province (Grant No. SKL202402004), the Jilin Province Major Science and Technology Program (Grant No. 20240211002GX), and the Open Research Fund of the Key Laboratory of Functional Materials Physics and Chemistry of the Ministry of Education (Jilin Normal University, Grant No. 202405).

References

[1] Zhao C X, Liu J N, Li B Q, Ren D, Chen X, Yu J and Zhang Q 2020 *Adv. Funct. Mater.* **30** 2003619
[2] Que Z Y, Wei Z C, Li X Y, Zhang L, Dong Y H, Qin M L, Yang J J, Qu X H and Li J 2022 *J. Mater. Sci. Technol.* **126** 203
[3] Dai F Z, Wen B, Sun Y J, Ren Y X, Xiang H M and Zhou Y C 2022 *J. Mater. Sci. Technol.* **123** 26
[4] Fahrenholtz W G and Hilmas G E 2017 *Scr. Mater.* **129** 94
[5] Sandeep K and Abhishek S 2023 *J. Inst. Eng. India Ser. D* **105** 1601
[6] Gasch M J, Ellerby D T and Johnson S M 2005 *Handbook of ceramic composites* (Springer, Boston) pp. 224
[7] Gan Q, Liu H T, Zhang S, Wang F, Cheng J, Wang X, Dong S S, Tao Q, Chen Y L and Zhu P W 2021 *ACS Appl. Mater. Interfaces* **13** 48
[8] Chen Y L, Yu G T, Chen W, Liu Y P, Li G D, Zhu P W, Tao Q, Li Q J, Liu J W and Shen X P 2017 *J. Am. Chem. Soc.* **139** 12370
[9] Li Z, Zhao B, Wang L, Tao Q and Zhu P W 2022 *J. Phys. Condens. Matter* **35** 074002
[10] Xu H Y, Ji W, Guo W M, Li Y L, Zou J, Wang W M and Fu Z Y 2022 *Adv. Sci.* **9** 2104532
[11] Koh Y H, Lee S Y and Kim H E 2001 *J. Am. Chem. Soc.* **84** 239
[12] Ma T, Zhu P W and Yu X H 2021 *Chin. Phys. B* **30** 108103
[13] Silvestroni L, Sciti D and Bellosi A 2007 *Adv. Energy Mater.* **9** 915
[14] Zhang H, Springer H, Aparicio Fernández R and Raabe D 2016 *Acta Mater.* **118** 187
[15] Liu J G, Li Y, Cheng C G and Li W 2024 *J. Aust. Ceram. Soc.* **60** 971
[16] Liu J X, Peng F, Ma G L, Liang W J, He R Q, Guan S X, Tang Y and Xiang X J 2023 *Chin. Phys. B* **32** 098101
[17] Mondal S, Chakraborty S and Das S 2018 *J. Mater. Eng. Perform.* **27** 6040
[18] Bakshi S R 2016 *Technologies* **4** 30
[19] Chakraborty S, Debnath D, Mallick A and Das P K 2014 *Int. J. Refract. Met. Hard Mater.* **46** 35
[20] Inagaki J I, Sakai Y, Uekawa N, Kojima T and Kakegawa K 2007 *Mater. Res. Bull.* **42** 1019
[21] Gu X L, Liu C, Gao X X, Zhang K, Zheng W T and Chen C F 2023 *Research* **6** 35
[22] Aronsson B 1960 *Mod. Mater.* **143** 90
[23] Demirskyi D, Solodkyi I, Nishimura T and Vasylkiv O O 2019 *J. Am. Ceram.* **102** 4259
[24] Akarsu M K and Akin I 2021 *J. Alloys Compd.* **884** 161110
[25] Neuman E W, Thompson M, Fahrenholtz W G and Hilmas G E 2021 *J. Eur. Ceram. Soc.* **41** 7434
[26] Li N N, Li H, Tang R L, Han D D, Zhao Y S, Gao W, Zhu P W and Wang X 2014 *Chin. Phys. B* **23** 046105
[27] Kong Q Y, Huo S J, Chen L, Wang Y J, Ouyang J H and Zhou Y 2022 *Ceram. Int.* **48** 17981
[28] Zhang X R, Zhang Z X, Wang W M, Shan J H, Che H W, Mu J B and Wang G S 2017 *J. Am. Ceram.* **100** 3099
[29] Zuo Y, Liu Z B, Zhao W, Liu Y, Gai X M, Han D D, Wang X, Dong S S, Tao Q and Zhu P W 2023 *Int. J. Refract. Met. Hard Mater.* **110** 105997
[30] Zhao F, Tao Q, You C, Ye M Y, Li L, Han Y, Dong S S, Wang X, Cui T and Zhu P W 2020 *Mater. Chem. Phys.* **251** 123188
[31] Zdaniewski W A 1987 *J. Am. Ceram.* **70** 793
[32] Cao P P, Huang H L, Jiang S H, Liu X J, Wang H, Wu Y and Lu Z P 2022 *J. Mater. Sci. Technol.* **122** 243
[33] Huang H L, Sun Y, Cao P P, Wu Y, Liu X J, Jiang S H, Wang H and Lu Z P 2022 *Scr. Mater.* **211** 114506
[34] Sagar K and Suresh P 1981 *J. Am. Ceram.* **64** 533
[35] Shen X L, Wu K P, Sun H Y, Sang L W, Huang Z H, Imura M, Koide Y, Koizumi S and Liao M Y 2021 *Diamond Relat. Mater.* **116** 108403
[36] Wang Y, Zhang G H, He X B and Yan B J 2019 *Ceram. Int.* **45** 15772
[37] Ye S B, Zhu J P, Li P C, Li M L, Yan N and Wang H L 2023 *Mater. Today Commun.* **34** 105228
[38] Liu B Q, Cui G D, Sun J, Qiao J J and Zhang L L 2024 *Ceram. Int.* **50** 1874
[39] Chen F, Yan K, Zhu Y S and Hong J 2022 *Ceram. Int.* **48** 28774
[40] Simonenko E P, Simonenko N P, Sevastyanov V G and Kuznetsov N T 2016 *Russ. J. Inorg. Chem.* **61** 1483
[41] Zapata S E, Jayaseelan D D, Lin H T, Brown P and Lee W E 2013 *J. Eur. Ceram. Soc.* **33** 1373
[42] Bhaumik S K, Diwakar C, Singh A K and Upadhyaya G S 2000 *Mater. Sci. Eng. A* **279** 275